Discrete element simulation and experimental study of powder spreading process in additive manufacturing

Powder Technology 306 (2016) 45–54

Contents lists available at ScienceDirect

Powder Technology

journal homepage: www.elsevier.com/locate/powtec

Discrete element simulation and experimental study of powder spreading process in additive manufacturing

S. Haeri[a,*], Y. Wang[b], O. Ghita[b], J. Sun[c]

[a] Department of Mechanical and Aerospace Engineering, University of Strathclyde, Glasgow G1 1XJ, UK
[b] College of Engineering, Mathematics and Physical Sciences, University of Exeter, North Park Road, EX4 4QF, UK
[c] School of Engineering, University of Edinburgh, Edinburgh EH9 3JL, UK

ARTICLE INFO

Article history:
Received 26 July 2016
Received in revised form 10 October 2016
Accepted 5 November 2016
Available online 9 November 2016

Keywords:
Additive manufacturing
Discrete element method
Laser sintering
3D printing
Powder spreading

ABSTRACT

Powders used in additive manufacturing (AM) are spread onto a compact layer of particles for sintering and this process is repeated layer by layer to form the final products. Spreading of rod-shaped particles in realistic AM settings is simulated using the discrete element method (DEM) to investigate the effects of particle shape and operating conditions on the bed quality, characterised by its surface roughness and solid volume fraction. It is discovered that larger particle aspect ratios, A_r, or higher spreader translational velocities result in a lower bed quality, i.e. a larger surface roughness and a smaller volume fraction. The surface roughness increases monotonically with A_r. However, the volume fraction exhibits a maximum at $A_r = 1.5$ for randomly packed powder beds that are formed by the roller type spreaders moving at low translational velocities. It is also found that a roller outperforms a blade spreader in terms of the quality of the prepared bed at the same operating conditions. The micro-structural analysis of the beds also shows particle alignment in response to the induced flow, which is qualitatively confirmed by a set of purposely-designed experiments. In addition, a shape segregation is documented for powders with mixed aspect ratios (A_r) such that particles with larger A_r tend to accumulate on the upper layers of the bed.

1. Introduction

Additive manufacturing has recently been exploited by various industries, such as automotive, aerospace and medical, as a novel production technology. Powder bed laser sintering (LS) or laser fusion is one of such promising AM techniques. It uses polymeric or metallic particles, heated to just below their melting temperature and spread on a fabrication piston to form a thin particle bed using a counter-rotating roller or a blade. A laser beam is then focused onto the bed and scans a raster pattern of a single layer of the final part. After sintering the fabrication piston lowers the part slightly and a new layer of powder is applied. The process is repeated until the product is successfully fabricated [1].

The technology offers substantial benefit for rapid production of prototypes and more recently for weight-sensitive/multi-functional final parts at small-volumes, with almost arbitrary complexity [2]. There is a growing demand for adoption of the technology. However, insufficient understanding of the multi-physics processes involved in the LS which comprise granular flow (spreading), heat transfer, phase change and surface phenomena, is hindering further development of the technology and introduction of new materials [3]. Such limitations result in expensive trial-and-error calibrations, uncertainty in the quality of final products and slow production rates due to interrupted builds.

The spreading process has a major impact on the characteristics and quality of the final product. The determining parameters are the solid volume fraction of the bed and smoothness of its surface since higher porosity or large roughness can lead to weaker bonding between layers and hence a poor mechanical performance. The importance of the layer smoothness and compactness has been demonstrated by Berretta et al. [4] using a new grade of Poly-Ether Ether Ketone (PEEK) in various spreading experiments. Ziegelmeier et al. [5] also reported strong connection between the powder volume fraction and the porosity of the sintered parts. They also demonstrated that the part's surface quality is highly dependant on the roughness of the powder bed.

The first analytical model, close to the LS method of operation, was developed by Johanson [6] to predict the behaviour of granular materials undergoing continuous shear between two rollers (see T-Dec et al. [7] for a review), and has been extended to compaction between a roller and a flat plate [8]. These models, however, treat

* Corresponding author.
E-mail addresses: sina.haeri@strath.ac.uk (S. Haeri), Y.Wang@exeter.ac.uk (Y. Wang), O.Ghita@exeter.ac.uk (O. Ghita), j.sun@ed.ac.uk (J. Sun).

http://dx.doi.org/10.1016/j.powtec.2016.11.002

powder beds as continuous media described by macroscopic conservation equations to calculate quantities such as stress distribution or bulk density within the bed. Therefore, the effects of particle shape and micro-structure on bed quality cannot be directly evaluated.

The development and performance of new material for the LS have also been the subject of a few experimental studies without linking to the spreading process itself. For instance, Wang et al. [9] studied the mechanical and thermal properties of graphite platelet reinforced PEEK (PEEK/GP). They showed that despite a higher porosity, the tensile strength of the composites is improved (maximum 36% improvement for 5 wt.% GP). Wang et al. [10] also studied the laser sintered glass bead filled Polyether ketone (GB/PEK) composites and showed up to 7% increase in hardness can be achieved without reducing its tensile strength.

Recently the DEM has been applied to the spreading problem to investigate the effects of particle level phenomena on the bed quality. Partelia and Pöschel [11] performed full device DEM simulations and found that the larger translational velocity of the roller and broader particle size distribution lead to larger surface roughness. Xiang et al. [12] simplified the process by considering an assembly of 4000 spherical particles undergoing three processes in their DEM simulations: random packing, layering and compression. Focusing on the effects of particle size distribution and considering monosized, bimodal and Gaussian distributions of spherical particles, they showed that the solid volume fraction increases with layer thickness regardless of the size distribution type.

In this paper, the spreading of *non-spherical* particles in AM is studied using DEM simulations. A commercial grade and two types of custom-milled PEK/PEEK powder particles are characterised experimentally. Based on these experiments rod-shaped particles are chosen for the simulations. The effects of spreading devices (roller or blade), their translational velocity and the bed thickness on the surface roughness and bed volume fraction are identified. It is found that a larger translational velocity generally reduces the bed quality and hence a lower value is suggested. This will however, adversely affect the production rate. In addition, it is found that the rollers produce powder beds with significantly better qualities and this is related to the contact dynamics between the spreader and the bed. The bed micro-structure in terms of particle orientation is analysed and an alignment phenomenon is observed and related to the bed response to the particle shape and the spreader velocity. Spreading experiments with rod particles are performed to qualitatively validate the particle alignment phenomenon. Finally, a mixture of rod-shaped particles with different aspect ratios is considered to study the shape segregation phenomenon. This analysis show that mixing particles with different shape/size distributions to control the bed quality may not be effective due to particle segregation in different layers of the bed.

It is also important to note that Parteli and Pöschel [11] earlier used similar DEM techniques to simulate the same process – admittedly with more realistic particle shapes. However, in this paper we have performed extensive parametric studies to characterise the process. Several adjustable parameters, available to device users, which are commonly used for tuning the process are considered and their effects on the bed quality are documented. In addition, we believe this is the first study that uses detailed micro-structural analysis to explain the complex dependence of bed quality on the aforementioned adjustable parameters and also on particle shape (at least for elongated particles).

2. Particle shape characterisation

PEK, PEEK and their composites have received significant attention in AM recently due to their good strength, stiffness, thermal, mechanical and chemical resistance [4,9,13-17]. This motivated us to characterise the shape of three different variations of these particles. This will also provide the basis for choosing the particle shapes in our numerical simulations. The commercial grade EOS HP3 PEK in addition to disk- and impact-milled 450G PEEK particles are considered. A cryogenic pulveriser (Powder King PKA-18) composed of a stationary and a rotating (at 30 Hz) disk with their gap set to 0.127 mm and its chamber cooled to −50 °C was used to disk-mill the grade 450G PEEK granules supplied by Victrex Plc. A 100 UPZII Universal Impact Mill (Hosokawa, Germany) operating at room temperature with a 2 mm sieve size and a blade rotation speed of 14,000 rpm was used for the impact milling.

The shape characterisation was performed in ImageJ software [18] analysing images obtained using a Scanning Electron Microscope (SEM) device (Hitachi S-3200N) under 20 kV acceleration voltage and with all samples coated with a 10 nm gold/palladium layer. Fig. 1 shows the results of this analysis. For the EOS HP3 PEK, both sphericity $\mathcal{S}$ and roundedness $\mathcal{R}$ are accumulated in the interval $[0.6, 0.8]$ showing properties of elongated particles with round edges. Aspect ratios are concentrated around $A_r = 1.5$ with a notable tail extending to a $A_r = 3.0$. Impact milled PEEK particles have the highest degree of sphericity $\mathcal{S} \approx 0.9$ and regularity with nearly 90% of particle having $A_r \approx 2$. The disk-milled particles are quite irregular with the sphericity and roundedness spread between $0.2 < \mathcal{S} < 0.85$ and $0.15 < \mathcal{R} < 0.95$ respectively. However, accumulation on a diagonal line still characterises elongated particles and in fact the aspect ratio histogram shows a wide log-normal like distribution with mean value $A_r \approx 2.5$ and a tail extending to $A_r = 5$.

The results of these analyses show that elongated particles with a major axis and round edges are good approximations to the milled PEK/PEEK particles. Therefore, rod-shaped particle generated with a multi-sphere approach are chosen for the simulations (see Section 3.1).

3. Methodology

In this section the DEM technique is discussed first. Then the simulation and post-processing procedures are specified and their parameters are discussed in the relevant sections in detail. Nevertheless, a summary of important simulation/post-processing parameters is provided in Table 1 for reference.

3.1. Discrete element method

The Large-scale atomic/molecular massively parallel simulator (LAMMPS) code [19] is used for all the DEM simulations in this paper. Firstly, note that a distinction between a sphere and a particle is made since we will consider non-spherical particles created with a set of spheres. Therefore, a spherical/non-spherical particle is formed from one/or more spheres. A linear Hookean spring-dashpot contact force model is applied to each pair of spheres p and q whenever the two spheres overlap, i.e. when $\delta_{pq} = R_p + R_q - r_{pq} > 0$, where $r_{pq} = \| r_{pq,i} \| = \| r_{p,i} - r_{q,i} \|$[1], and $\| \cdot \|$ represents the Euclidean norm (magnitude) of any vector. In addition, R_k, $k \in \{p, q\}$, is the radius of the kth sphere and $r_{k,i}$ is the position vector of its centre of mass (CoM). The normal and tangential components of spring-dashpot force are given by

$$F^n_{pq,i} = \kappa_n \delta_{pq} n_{pq,i} - \gamma_n m^* v^n_{pq,i} \tag{1}$$

$$F^t_{pq,i} = -\kappa_t u^t_{pq,i} - \gamma_t m^* v^t_{pq,i}, \tag{2}$$

[1] A tensor notation is adopted throughout this paper. For example $r_{p,i}$ with $i \in \{1, 2, 3\}$, is the position vector of sphere "p".

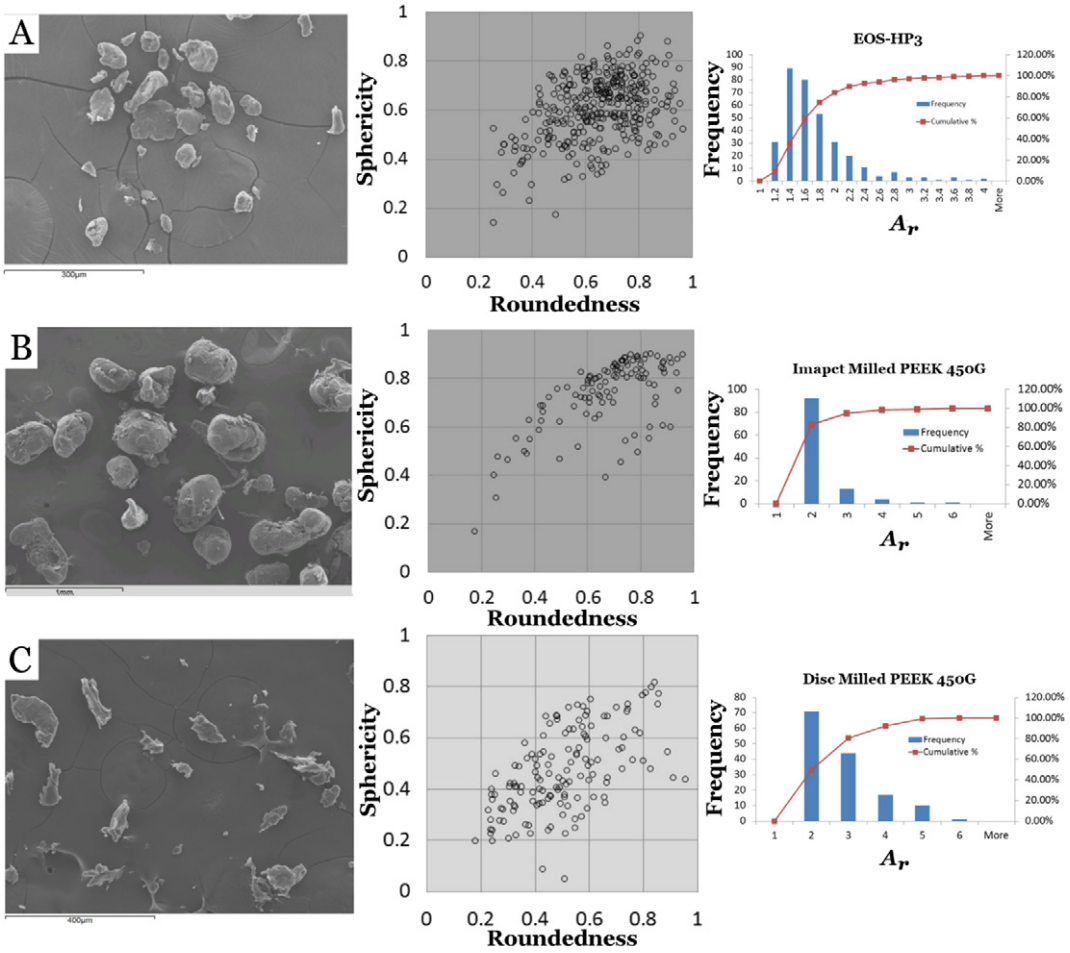

Fig. 1. Characterisation of particle shapes for (A) EOS HP3 PEK, (B) impact-milled PEEK and (C) disk-milled PEEK. For each particle type a representative SEM image, sphericity versus roundedness and also the aspect ratio distribution is presented.

where $\kappa_n, \gamma_n, \kappa_t$ and γ_t are spring elastic and damping constants in normal and tangential directions respectively. In addition, $v^n_{pq,i}$ and $v^t_{pq,i}$ are relative normal and tangential velocities. The effective mass is defined as $m^* = m_p m_q/(m_p + m_q)$ where m_k, $k \in \{p, q\}$, is the mass of kth sphere. The unit normal vector in the direction of the line connecting a pair of sphere centres is presented by $n_{pq,i}$ and elastic shear displacement by $u^t_{pq,i}$. The tangential force is limited to $\left\|F^t_{pq,i}\right\| \leq \mu_c \left\|F^n_{pq,i}\right\|$ where μ_c is the Coulomb friction coefficient. Similarly, a normal $F^n_{pw,i}$ and a tangential force $F^n_{pw,i}$ are defined between sphere p and the bottom wall w.

The spring-dashpot model is chosen in this study due to its low computational costs. Despite the simplicity of the model, Di Renzo and Di Maio [20] showed that if the parameters of the model are accurately chosen, the model performs as well as the full Hertz-Mindlin and Deresiewicz model – and better than the simpler versions of this model – as long as the details of collision forces are not relevant (for example in particle breakage). In this study we are only considering the dynamics of the bed and hence the use of linear model is justified. The details of calculating model parameters are discussed later in this section.

The DEM is traditionally formulated for spherical particles which is due to the availability of efficient collision detection algorithms and well defined tangential and normal contact forces (Eqs. (1) and (2)). However, shape effects are considered in this paper and hence, a versatile multi-sphere technique is used, see Fig. 2. The contacts are still detected between sphere pairs in this technique. However, instead of integrating the Newton's laws of motion for each sphere, a total force and torque around the CoM of each non-spherical (here rod-shaped) particle is calculated by adding-up individual contact

Table 1
A summary of simulation and post processing parameters with a short description. This is provided only for reference and the parameters are explained in detail in the text. In addition, all the dimensional parameters are reported in SI units.

Parameter	Description	Value
κ_n	Normal Spring Constant	1500
E	Coefficient of Restitution	0.5
γ_n	Normal Dash-pot Constant	Eq. (5)
κ_t	Tangential Spring Constant	$2/7\kappa_n$
γ_t	Tangential Dash-pot Constant	$1/2\gamma_n$
μ_r	Rolling Friction Constant	0.005
D_{sph}	Sphere diameter (for rods)	10^{-4}
ρ_{rod}	Particle Density	1300
ℓ	Sphere Overlap	0.5 (in simulations)
m_{sph}	Sphere's Mass	Eqs. (6) and (7)
A_r	Aspect ratio	$\in \{1.0, 1.5, 2.0, 2.5\}$
L_x, L_y, L_z	Domain size in x, y, z	$2.46 \times 10^{-3}, 0.04, 0.03$
δ_{init}	Layer thickness (before spreading)	$10D_{\text{sph}}$
$D^r_{\text{sph}}, D^b_{\text{sph}}$	Sphere diameter (roller/blade)	5.026×10^{-5}
δ_{spreader}	Spreader Displacement	$\in \{4, 5\}D_{\text{sph}}$
D_{roller}	Roller Diameter	$200D_{\text{sph}}$
$z_{\min}$	Bottom Plane Location	Not relevant
$y_{\min}, y_{\max}$	Min/Max Particle Location in y	Sim. Dependent
z_{lo}, z_{hi}	Box Extent in z (post-process)	$z_{\min}, z_{\min} + \delta_{\text{spreader}} - 1.5D_{\text{sph}}$
y_{lo}, y_{hi}	Box Extent in y (post-process)	$y_{\min} + D_{\text{roller}}, y_{\max} - D_{\text{roller}}$

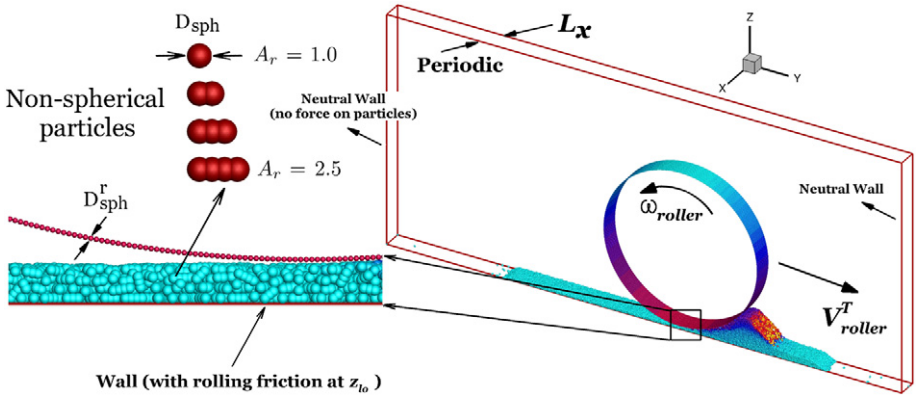

Fig. 2. A representation of the device simulation set-up. The non-spherical (rod-shaped) particles with different aspect ratios A_r, which are approximated using a multi-sphere technique are presented. The particles are coloured in the representative simulation (on the right) with their velocity magnitude. A section of the spreader with a width L_x is simulated.

forces of its constituent spheres. The CoM position of each rod is then updated using Newton's laws of motion and the location of individual spheres is updated assuming rigid-body dynamics.

The simulation set-up is depicted in Fig. 2. The bottom boundary is a rigid wall that exerts a normal and a tangential force on the spheres (equivalent to assuming an infinity large sphere in Eqs. (1) and (2)). To prevent unbounded rotation of particles on the bottom wall, a rolling friction model is implemented. The adopted model constantly applies a resistive torque to the spheres in contact with the bottom wall, which is given by [21–23]

$$T_{pw,i} = -\mu_r R_p \left\| F^n_{pw,i} \right\| \frac{\omega_i^{\text{rel}}}{\left\| \omega_i^{\text{rel}} \right\|}. \tag{3}$$

In Eq. (3) ω_i^{rel} is the relative angular velocity between particle p and the bottom wall w and $\mu_r = 0.005$ is used for all the simulations. This value is chosen based on the analysis of Zhou et al. [21] to yield a travelling distance of approximately $10D_{\text{sph}}$. Particles are usually spread on previous layers which are not smooth. Therefore, it is not expected that particles freely roll for long distances. In the absence of experimental measurements this is a reasonable assumption. In addition, this parameter mainly affects the characteristics of the bed on the edges – where significant rolling may take place – which are excluded from post-processing (see Section 3.3 .)

The elastic spring constant κ_n, in Eq. (1) is set according to [20]

$$\kappa_n = \frac{16}{15}\sqrt{R^*}Y^*\left(\frac{15m^*V_c^2}{16\sqrt{R^*}Y^*}\right)^{\frac{1}{5}}, \tag{4}$$

and the dash-pot constant is calculated as

$$\gamma_n = \sqrt{\frac{4\kappa_n(\ln E)^2}{m^*[\pi^2 + (\ln E)^2]}}, \tag{5}$$

where $1/R^* = 1/R_p + 1/R_q$, $1/m^* = 1/m_p + 1/m_q$, $1/Y^* = \left(1-\nu_p^2\right)/Y_p + \left(1-\nu_q^2\right)/Y_q$. In addition, Y, E, ν and V_c are the Young's modulus, coefficient of restitution, Poisson ratio and a characteristic velocity respectively. The coefficient of restitution is set to 0.5. The values of Young's modulus and Poisson ratio are set to 3.7 GPa and 0.4 for all particles which are typical values for PEEK polymeric particles [24]. Assuming $V_c = V^T_{\text{roller}}$ (or V^T_{blade}), Eq. (4), yields $\kappa_n \approx$ 1500N/m depending on the roller velocity. Therefore, a constant value of $\kappa_n = 1500$ is adopted for all the simulations. Tangential force constants κ_t and γ_t are respectively set to $2/7\kappa_n$ and $1/2\gamma_n$ (see Shäfer et al. [25] for details). Note that the mass of each individual sphere is adjusted in the simulations by

$$m_{\text{sph}} = \rho_{\text{rod}} V_{\text{rod}} / N_{\text{sph}}, \tag{6}$$

such that the density of all particles shapes remain equal to $\rho_{\text{rod}} = 1.3\ \text{gr/cm}^3$, (i.e. the PEEK density [24]). The analytical volume of rod-shaped particles is derived as

$$V_{\text{rod}} = \frac{N_{\text{sph}}\pi D^3_{\text{sph}}}{6} - \frac{2(N_{\text{sph}}-1)\pi h^2}{3}\left(\frac{3D_{\text{sph}}}{2} - h\right), \tag{7}$$

where, $h = \ell D_{\text{sph}}/2$, D_{sph} is the sphere diameter and N_{sph} is the number of spheres that constitute the rod and ℓ is the amount of overlap relative to D_{sph} between the spheres ($\ell = 0.5$ for all rod-shaped particles use in the simulations, see Fig. 2). Due to this adjustment of masses, γ_n values in Eq. (5), are calculated for rods with different aspect ratios based on their corresponding m^*.

3.2. Simulation set-up

Rods with various aspect ratios $A_r = 1.0, 1.5, 2.0, 2.5$ are created by overlapping spheres with $\ell = 0.5$ (Fig. 2). The initial configuration (before the spreading starts) is prepared by pouring randomly generated particles within a simulation box with dimensions $L_x = 2.46 \times 10^{-3}$, $L_y = 0.04$ and $L_z = 0.03$ on the bottom wall. Note that all values are in SI units except otherwise stated. The geometric parameters L_x, L_y and L_z are the width, length and height of the simulation box (red boundaries in Figs. 2 and 3). The box size in flow-direction L_y changes to accommodate all particles as they are spread and the left and right walls (in y-direction) exert no force on the particles. The number of rods in each simulation is adjusted to supply an initial thickness of $\delta_{init} \approx 10D_{\text{sph}}$ for all particle types. During the spreading process the height of the powder heap accumulated in front of the spreader may reach to half its diameter/height or slightly more. The value of δ_{init} is chosen such that the height of the front particle heap remains bounded to $1/2D_{\text{roller}}$.

The spreader is simulated using a set of rigidly moving spheres. A roller is created using 61250 spheres with $D^r_{\text{sph}} = 5.026 \times 10^{-5}$ that move with predefined translational V^T_{roller} and rotational $\omega_{\text{roller}} = 2V^T_{\text{roller}}/D_{\text{roller}}$ velocities. Similarly, a blade is created with 98,000 particles $\left(D^b_{\text{sph}} = D^r_{\text{sph}}\right)$ and a thickness of $10D^b_{\text{sph}}$ ($D_{\text{sph}}{}^b = D_{\text{sph}}{}^r$) which moves with a constant translational velocity V^T_{blade}. This set-up requires 1.6–1.9 × 10^5 spheres depending on the shape of particles

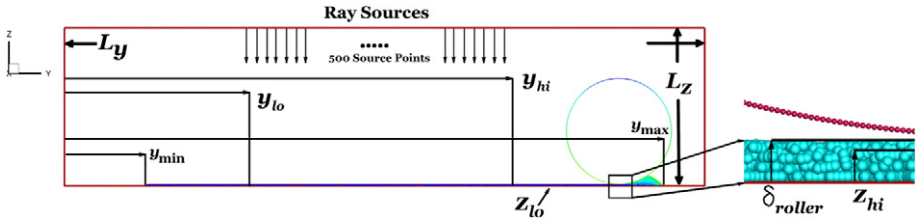

Fig. 3. Definition of parameters used in the post processing. The bed thickness, δ_{roller} and the geometric parameters $y_{\min}, y_{\max}, y_{lo}, z_{hi}, z_{lo}$ are presented. The ray's locations and the domain extent in y- and z-directions (L_y, L_z) are shown in this figure. These parameters are defined similarly for the cases with a blade spreader.

(i.e. different A_r). The simulations are performed for mono- or poly-dispersed particles where rods with $A_r = 1.5, 2.0, 2.5$ are mixed with fractions 0.5 : 0.35 : 0.15. It is worth mentioning that in this paper we are only considering shape effects. Therefore, the term "poly-disperse" refers to particles with different aspect ratios.

3.3. Post-processing

The particle volume fraction, ϕ, and surface roughness ϵ of the bed are investigated in this paper and used as a measure for effectiveness of the spreading process. This is defined by a high ϕ (close to the critical volume fraction) and a low ϵ value (smooth surface). It is in fact, possible to incorporate both parameters in a single variable. If the particles bounded by the bottom wall and a plane tangent to the top particle layer (i.e $\delta_{\text{spreader}} = z_{hi}$, where spreader $\in$ {roller, blade}) are considered, a larger roughness would be equivalent to a smaller ϕ. However, here the first approach is taken since a single value will be too sensitive to how the tangent plane is defined. Therefore, to calculate ϕ those particles that are bounded in a box defined by $z_{lo} = z_{\min}$, $z_{hi} = z_{\min} + \delta_{\text{spreader}} - D_{\text{sph}}$, $y_{lo} = y_{\min} + D_{\text{roller}}$ and $y_{hi} = y_{\max} - D_{\text{roller}}$ are selected. Here, δ_{spreader} is the roller displacement from the bottom (required layer thickness), see Fig. 3. For consistency y_{lo} and y_{hi} are defined with D_{roller} for both types of spreaders. Also, $y_{\min}$ and $y_{\max}$ are the minimum and maximum locations of particles on the bottom wall along y-direction. Defining y_{lo} and y_{hi} effectively limits the analysis to only a subset of particles away from the edges and suppresses the end effects. In fact, this is a reasonable assumption since the full extent of the bed in not normally used for fabrication. Table 2 summarises the effects of y_{lo} location on the value of ϕ. Near the edges ϕ is a strong function of y_{lo} as expected. However, by adding a displacement of D_{roller} the edge effects are satisfactorily suppressed.

It is worth mentioning that to manage the computational costs, a $D_{\text{roller}}/D_{\text{sph}} = 200$ is adopted with $D_{\text{sph}} = 0.1$ mm which is smaller, but of the same order of magnitude of the typical ratio $D_{\text{roller}}/D_{\text{sph}} \approx 500 - 1000$ used in a LS device. The chosen ratio is also tested to confirm that it is large enough to guarantee independence of the results.

The surface roughness ϵ is measured using a ray-tracing technique where 10 rows (in x-direction) of light sources are evenly distributed on the top plane. Each row consists of 500 equally distanced sources (see Fig. 3) in y-direction which provides 5000 data points in total. Each ray intersects the bed at a specific height h and the standard deviation of h normalised by D_{sph}, is defined as a roughness i.e. $\epsilon = \sqrt{\langle (h - \langle h \rangle)^2 \rangle}/D_{\text{sph}}$ where averages are calculated over all data points.

For micro-structural analysis in Section 4.2 an orientation vector – a unit vector g_i, in the direction of particle's major axis – is defined, see Fig. 6a. In addition, a probability density function (PDF) for spatial distribution of orientation vectors g_i can be defined according to [26]:

$$\mathcal{P}(g_i) = \frac{1}{4\pi}\left(\mathcal{D} + \mathcal{D}_{ij} g_i g_j + \mathcal{D}_{ijk\ell} g_i g_j g_k g_\ell + \cdots\right), \tag{8}$$

where equations for $\mathcal{D}_{i_0 \cdots i_n}$ tensors of order $n = 0 \cdots 6$ can be found in [26]. For the current analysis, $\mathcal{P}(g_i)$ has been reconstructed up to the fourth-order.

4. Results and discussions

4.1. Bed quality

In this section, the effects of particle shape on the bed solid volume fraction ϕ are investigated. The results of these simulations are presented in Fig. 4a. First note that for all roller simulations a maximum volume fraction is observed at $A_r = 1.5$ which is independent of δ_{roller} and is more pronounced at lower V^T_{roller}. This behaviour closely follows the predictions of the random-packing theory for spherocylinders [27]. Similar dependency of ϕ on A_r are also observed in experiments on random-packing of ellipsoids [28]. After this peak, ϕ declines consistent with the trend of the random close packing density against aspect ratio. For a given particle shape, the key control parameter is found to be V^T_{roller} which can significantly influence the bed quality. It is shown that a higher roller translational speed yields a bed with higher imperfections on the surface and a smaller density (Fig. 4). These are the indications of a poor spreading which ultimately results in poor mechanical performance. Of course, the smallest possible V^T_{roller} cannot practically be applied since there is a trade-off between the production rate and the quality. Therefore, optimal values should be chosen depending on the operational constraints.

The ϵ values are plotted on Fig. 4b. Interestingly, for spherical particles, ϵ is a weak function of V^T_{roller} but by increasing A_r this functionality becomes much stronger. The investigation of micro-structural characteristics of the system is provided in the next section which illuminates the complex response of ϵ to the investigated parameters. The same behaviour is observed for δ_{roller} which has negligible effects on the roughness for $A_r \leq 1.5$ but the effects become stronger as A_r increases.

Two different cases are also considered for a blade spreader with $V^T_{\text{blade}} = 0.03$, $\delta_{\text{blade}} = 5D_{\text{sph}}$ and $V^T_{\text{blade}} = 0.04, \delta_{\text{blade}} = 4D_{\text{sph}}$.

Table 2
Independence of the results from the choice of y_{lo}. The results are obtained for the case with $A_r = 2.0$, $V^T_{\text{roller}} = 0.03$ and $\delta_{\text{roller}} = 4D_{\text{sph}}$. The cut-off length is defined with reference to $y_{\min}$; e.g. a cut-off of $0.25D_{\text{roller}}$ means $y_{lo} = y_{\min} + 0.25D_{\text{roller}}$. The value $y_{lo} = y_{min} + D_{\text{roller}}$ is used for all the simulations. Similarly $y_{hi} = y_{\max} - D_{\text{roller}}$ is used to bound the post-processing box as explained in Section 3.3.

Cut-off	0	$0.25D_{\text{roller}}$	$0.5D_{\text{roller}}$	$0.75D_{\text{roller}}$	D_{roller}	$1.25D_{\text{roller}}$
ϕ	0.4123	0.4385	0.4683	0.5023	0.5109	0.5099

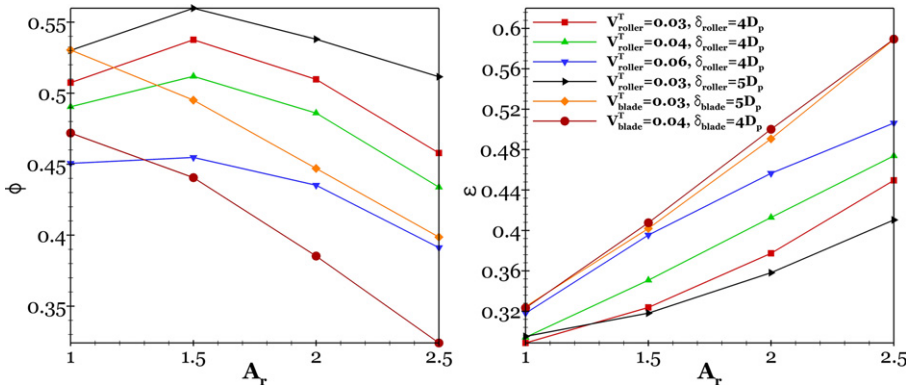

(a) Volume Fraction (b) Bed Roughness

Fig. 4. The effects of particle shape, V^T_{spreader}, δ_{spreader} and the spreader type on the bed quality. The quality is quantified by a volume fraction ϕ and a roughness parameter ϵ.

Firstly, note that the ϕ curve does not show a similar maximum at $A_r = 1.5$ and also a significantly larger ϵ is observed, see Fig. 4a and b, compared to the roller at the same operating conditions. The large surface disturbances generated by the blade penetrate as deep as z_{hi} (Fig. 3) and hence, in the volume selected for the calculation of ϕ, close packing characteristics are not observed. Secondly, note that the bed quality is seriously degraded (lower ϕ and larger ϵ) using a blade compared to a roller at same operating conditions. Fig. 5 shows a snapshot of both spreaders in contact with the bed. Clearly, the roller provides a large contact area and allows for gradual particle rearrangement. Conversely, the blade, mainly interacts with the bed at a single point (its edge), dragging the particles as it moves which leads to greater roughness ϵ. A larger A_r exacerbates the problem (see Fig. 4b) and a thicker blade does not solve the single point contact problem. Finally note that, an increase in V^T_{blade} and reduction of δ_{blade}, similar to the roller case, significantly reduce the volume fraction ϕ but have a milder effect on ϵ. This is perhaps due to the dominant dragging effect as explained earlier. Note that, for example for $A_r = 2.5$, the roughness reaches a value of $0.59D_{\text{sph}}$ and physically this can not be substantially increased except if there are deep and wide cracks in the structure of the bed.

4.2. Microstructural analysis

4.2.1. Simulation results

In this section the micro-structural behaviour of particles undergone the spreading process is discussed. Fig. 6a shows the probability of finding the vector representing a rod's major axis within a 20° deviation from $\mathbf{e}_2 = (0,1,0)$ (i.e. the particle flow/spreading direction). Note that for an isotropic distribution of g_i, $\Pr_I(\zeta < |\alpha|)$ can be analytically derived as $1 - cos(\alpha)$. Now, setting $\alpha = 20°$, one obtains $\Pr_I(\zeta < |\alpha|) \approx 0.06$. Fig. 6a clearly shows that $\Pr_I(|\zeta| < 20°) < \Pr(|\zeta| < 20°)$ for all aspect ratios and hence, particles are aligned in flow direction. To show that this alignment occurs during the process the value of $\Pr(|\zeta| < 20°)$ is calculated for the initial particle configuration. Table 3 shows the result of this calculations. The initial $\Pr(|\zeta| < 20°)$ values are smaller than all the values reported in Fig. 6a, which confirms that the spreading process increases the alignment in the spreading direction. Similar alignment to the flow direction has also been reported in numerical simulations of simpler flow systems. For instance, Guo et al. [29,30] showed that elongated particles align in the flow direction in a simple shear flow.

The PDF of g_i expanded according to Eq. (8) is presented in Fig. 7. It should be noted that these surfaces are not probabilities (but probability densities) and are not directly comparable to the plotted values in Fig. 6a. Nevertheless, an alignment, specially from z-direction to the flow direction is evident. This anisotropy can clearly be observed in all cases but a planar isotropy (circular shape of the distribution on the $x-y$ plane) is somewhat maintained for $A_r = 1.5$ but is completely broken for $A_r > 1.5$ which results in a unique director in the direction of roller's motion.

Fig. 6a shows that the alignment is a strong function of particle shape. The above analysis also indicates that two different types of

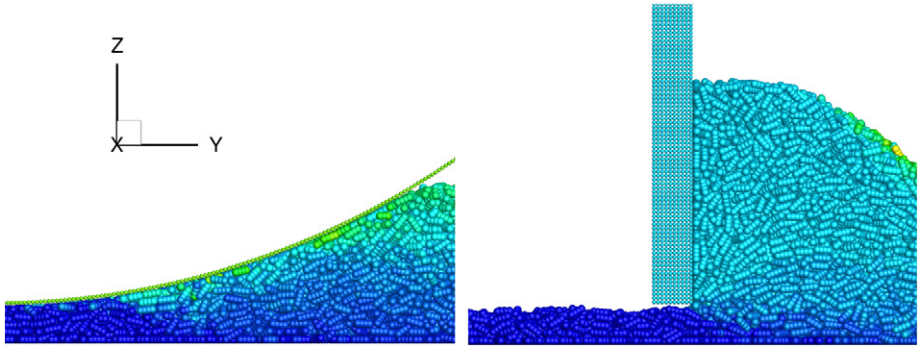

Fig. 5. The particle-spreader contact dynamics. A roller provides a better support for particles. The particles are coloured by their velocity magnitude.

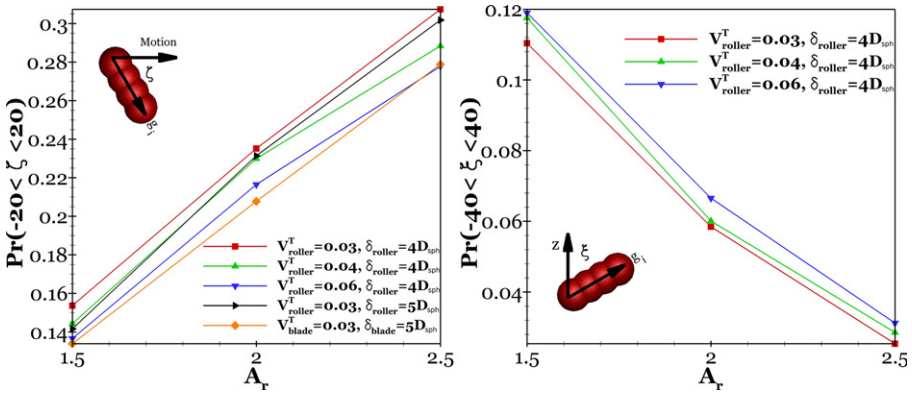

(a) The flow-direction (b) The z-direction

Fig. 6. The alignment of particle assemblies subjected to the spreading process. Probabilities in the flow- and z-direction are shown. To obtain meaningful statistics for the calculation of $\Pr(\xi < |\beta|)$, a larger threshold $\beta = 40^\circ$ is used since only a very small fraction of particles remain in this direction.

alignment take place. A first rotation (referred to as Type 1 hereafter), projects particles from the $z - x$ plane onto the $x - y$ plane but preserves the planar isotropy. The second one (Type 2), however, projects particles onto the flow direction. Particles with larger A_r experience a higher intensity of Type 2 rotations. The degradation of the bed quality with aspect ratio is believed to be related to the Type 2 rotations. These in-plane rotations can significantly disturb the nearby particles resulting in larger ϵ.

Fig. 6a shows that $\Pr(\zeta < |\alpha|)$ is a weak function of V^T_{roller} and decreases by increasing it. According to our argument, type 2 rotations result in higher ϵ. Here however, $\Pr(\zeta < |\alpha|)$ decreases by increasing V^T_{roller} while it is already observed that higher V^T_{roller} degrades the bed (Fig. 4). A distinction should be made between the two different types of rotation. This effect is related to the type 1 rotations; at high V^T_{roller} values a small fraction of particles simply do not have enough time to respond to the motion and do not align with the rest of particles on $x - y$ plane. This causes defects in the micro-structure resulting in higher ϵ and negating the effects of reduced $\Pr(\zeta < |\alpha|)$ values. Fig. 6b shows probability of finding particles in the proximity of z-axis, $\Pr(|\xi| < 40^\circ)$. The slight increase of $\Pr(|\xi| < 40^\circ)$ by increasing V^T_{roller} proves the argument.

The bed thickness, δ_{spreader} (only tested for the roller configuration) seems to result in a slightly less alignment in flow direction for all aspect ratios (less Type 2 rotation). This has an effect on the higher quality of the bed in line with the arguments in this section. However, larger δ_{spreader} is believed to also reduce the probability of particle congestion beneath the spreader and hence may have a mixed effect. Fig. 4 shows that the declination rate of ϕ increases after $A_r = 2.0$ for $\delta_{\text{roller}} = 4D_{\text{sph}}$ whereas, a constant slope is observed for $\delta_{\text{roller}} = 5D_{\text{sph}}$. Based on this observation, it is believed that a larger δ_{spreader} provides more space for smooth arrangement of particles beneath the spreader which becomes more significant at $A_r/\delta_{\text{spreader}} \geq 0.5$. It should be emphasised however, that this argument is based only on the limited available data and has not been investigated further in this study.

In Fig. 6a a curve for the blade case is also presented. Here again although the slightly lower alignment in flow direction may have a positive effect on the bed quality it is overshadowed by the particle dragging effect due to inefficient contact dynamics as explained in Section 4.1.

Table 3
The probability of finding a particle in alignment with the spreading direction in the initial configuration. Three initial configurations are prepared for different aspect ratios which are then used for all the corresponding simulations.

A_r	1.5	2.0	2.5
$\Pr(\lvert\zeta\rvert < 20^\circ)$	0.0878	0.0968	0.1097

4.2.2. Experimental results

The particle alignment is also explored experimentally. The experimental rig, consisting of a tray-roller system and rod-shaped particles are prepared using the LS process. The particle shape is equivalent to those presented in Fig. 2 but with $\ell = 0.25$. The manufacture of particles used in this experimental part was carried out using the EOSINT P100 system at a chamber temperature of 169 °C. The particles were manufactured from the EOS PA2200 (poly-amide) powder using a 16 W CO_2 lasers at 1500 mm/s scanning speed for post contour, and a 21 W CO_2 lasers at 2500 mm/s for hatching. The particles were then cooled down to room temperature before removal from the powder bed.

It should be noted that the experiments were mainly performed to support our simulations by showing that at a micro-structure level, the reported particle behaviour is also observed experimentally. We did not perform the experiments within a Laser Sintering device in this paper since other parameters would come into play, making the comparison even harder. Although we tried to build our experimental rig to operate as close as possible to the simulations/device conditions, the results are only qualitatively compared to the simulations.

A series of tests are carried out in the roller-tray system by spreading particles with either a roller or a blade. The tray was initially filled with white rod-shaped particles with $A_r = 2.5$ and 4.0. A mixed shape case with $A_r = 1.75, 4.0$ is also considered. Several black-coloured rods are manually placed on top of the bed, perpendicular to $\mathbf{e}_2$ on $x - y$ plane (assuming a coordinate system similar to the simulations). The spreading, was then carried out by moving the spreader with $V^T = 0.05$. The procedure is presented in Fig. 8. After exposing the buried black-coloured particles the particle orientation is measured and those with a maximum 20° deviation from $\mathbf{e}_2$ are considered as being aligned in the flow direction. Fig. 9 shows a snap-shot of the final particle configuration. The experiments are repeated 10 times and average orientations are summarised in Table 4.

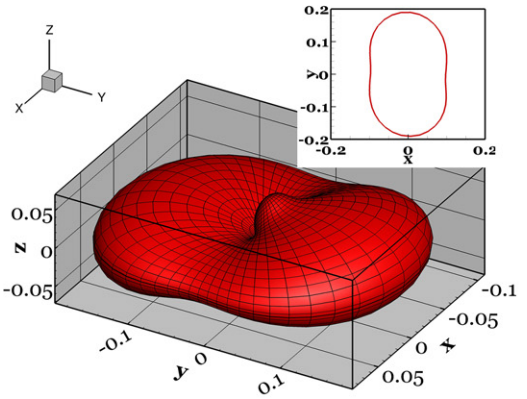

(a) $A_r = 1.5$

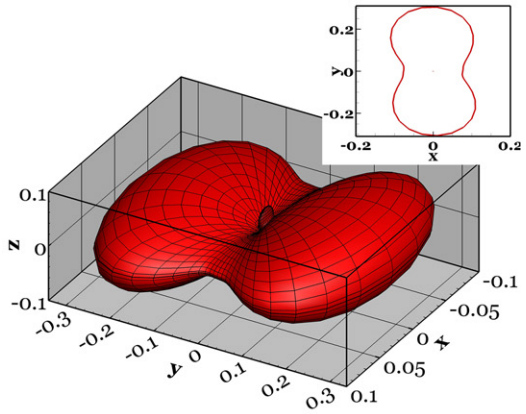

(b) $A_r = 2.0$

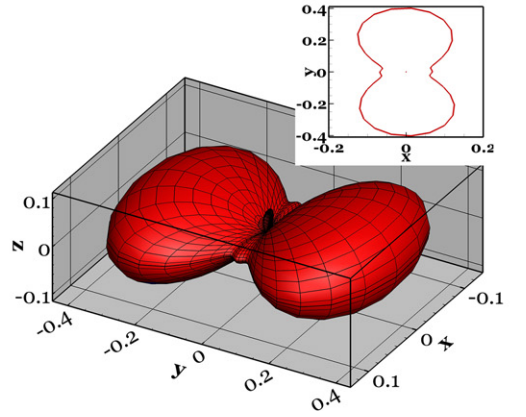

(c) $A_r = 2.5$

Fig. 7. The PDF of distribution of orientation vectors for $V^T_{\text{roller}} = 0.03$ and $\delta_{\text{roller}} = 5D_{\text{sph}}$. The projected PDF on the $x-y$ plane is also presented. A flat surface indicates a rotation onto the $x-y$ plane (Type 1). The Type 2 rotations cause the particles to align in the flow direction. This is evident in (b) and (c) where the surface is shrunk in the mid-section and forms two distinct lobes. Note also that the y-axis scaling is not identical in the three figures otherwise the effect would have been even more pronounced.

The experimental results in Table 4 show that the particle alignment is indeed a strong function of A_r. However, the effect of the spreading device is not conclusive. For mixed particles and for $AR = 4.0$, slightly larger alignment is observed for the blade whereas for $A_r = 2.5$, the roller generates a larger alignment. The discrepancy between values obtained from the experiments and simulations can be attributed to the differences in operating conditions and that only a specific sub-set of particles are tracked. Nevertheless, the experimental results, qualitatively confirm that the alignment indeed occurs and support the simulation results.

4.3. Shape segregation

So far only mono-disperse particle beds were considered for the parametric studies. In practice however, a distribution of different shapes is present. For rod-shaped particles this can be reduced to a distribution for A_r as presented in Fig. 1. A series of simulations are performed with $V^T_{\text{roller}} = 0.03, 0.04, 0.06$ for a mixture of three particle types $A_r = 1.5, 2.0, 2.5$, blended with the fractions 0.5, 0.35 and 0.15 respectively. Two major objective are pursued here: (1) to illuminate the effects of a shape distribution on characteristics of the final bed and (2) to explore whether the bed quality can effectively be controlled by manipulating the shape distributions, noting the non-linear response of the volume fraction to particle shape. For these simulations, the bed is prepared initially using the same protocol as mono-dispersed particles. The ratios are chosen to resemble the shape (parametrised with A_r) distribution of PEK/PEEK particles as discussed in Section 2.

Similar micro-structural behaviour is observed for the cases with a shape distribution to the mono-dispersed case. In fact, $\Pr(|\zeta| < 20^\circ) = 0.205$, 0.203 and 0.189 for $V^T_{\text{roller}} = 0.03$, 0.04 and 0.06. The particle alignment in beds composed of mixed shape particles is qualitatively confirmed with the experimental results, see Table 4. Also interestingly, the values of $\Pr(|\zeta| < 20^\circ)$ can be estimated accurately by a number density weighted average of the values of mono-shape particles at corresponding V^T_{roller}. These probabilities are calculated from the values presented in Fig. 6a, for $V^T_{\text{roller}} = 0.03, 0.04$ and 0.06 as 0.204, 0.195 and 0.185 respectively.

To fully characterise the bed however, the particle spatial distribution should be quantified. Our preparation protocol ensures an initial homogeneous distribution of different shapes in each layer. We defined 3 slabs over the bed thickness δ_{roller} centred at $(1/6, 1/3, 5/6)\delta_{\text{roller}}$ and calculate a probability for finding a certain particle type in each slab $\Pr_{\text{slab}}$. This is then normalised by a global number density $\Pr_g$ for each A_r which is calculated considering the entire bed. This normalisation is necessary to make the comparison possible and is defined such that a $\Pr_{\text{slab}}/\Pr_g = 1$ indicates no shape segregation. Fig. 10 show the distribution of A_r at three different slabs. It is clear that the probability of finding $A_r = 2.5$ in the bottom slab is only $0.75\Pr_g$ whereas, at the top slab it is increased to $1.24\Pr_g$. Conversely, for $A_r = 1.5$ the probability decreases from $1.12\Pr_g$ to $0.9\Pr_g$. This is a clear indication of shape segregation during the spreading process for the rod-shaped particles. It should be noted that, the particle shape is not isolated from its size and this in fact may be a mixed shape/size effect (since various shapes have different sizes). Nevertheless, this suggests that using particle shape manipulation to control volume fraction, may be ineffective since although the average solid volume fraction can be increased, it may not be distributed uniformly in different layers of the bed after the spreading.

5. Concluding remarks

The AM sector lacks materials. However, over the last couple of years the number of research studies on various polymeric powders for laser sintering increased. Many of the studies are using various milling methods to create powders and investigate their flow properties in relation to mechanical performance. Thus generated particles have large aspect ratios and irregular shapes. Understanding the effects of various morphologies is the key for introducing new certified material. Once a large number of certified material is available,

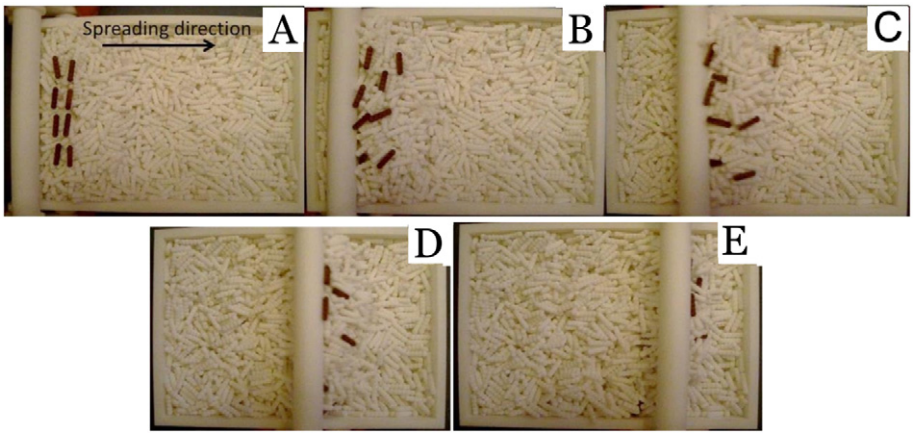

Fig. 8. A demonstration of the particle spreading experiments. After the spreading is complete, top particles are manually removed to expose the buried coloured particles.

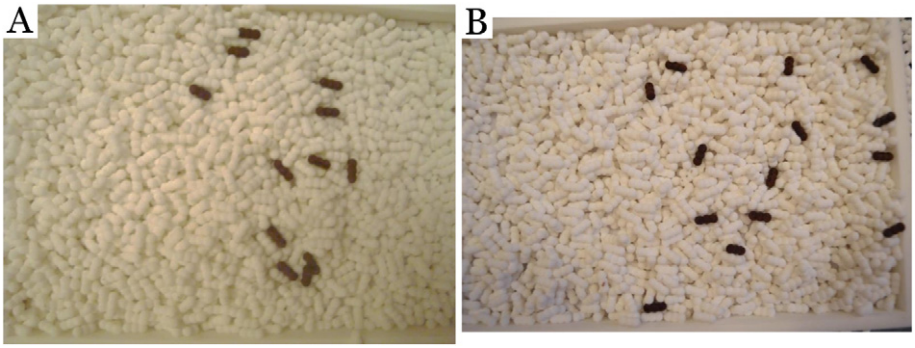

Fig. 9. Alignment of particles subjected to the spreading process. Two different spreader types are used: (A) roller, (B) blade.

composite powders will become of interest. Very often the powders and fibres are added together in a dry mix. No knowledge is currently available on optimal fibre size, length and aspect ratio for a high quality sintering process. This study provides insights into how new powders are going to perform in laser sintering.

To address these shortcomings, the effects of particle shape and spreading conditions on the powder bed characteristics, which are important factors determining the final product quality, are investigated. It is discovered that generally, particles with larger A_r result in a lower density powder bed with higher surface roughness and hence lower mechanical performance of the fabricated parts. An effective control parameter, considering the production time constraints, can be the spreader translational velocity V^T_{spreader}, the lower of which the better powder bed quality. It is also found that in the same operating conditions a roller type spreader significantly outperforms a blade. This has been attributed to inadequate contact of a blade with the bed, which causes particle dragging and degrades the bed quality.

A non-linear response of the volume fraction to the particle shape (with a maximum at $A_r = 1.5$) can also be exploited to control the bed quality by using non-spherical particles with an average A_r as close as possible to 1.5. However, it is found that for a mixture of particles with different A_r a mild shape segregation occurs which may negate such advantages gained by manipulating particle shape distribution.

Table 4
Average and standard deviation of measured probability of particle alignment in the flow direction. The statistics are calculated for 10 separate experiments.

Particle shape	$A_r = 2.5$		$A_r = 4.0$		Mixed, $A_r = 1.75, 4.0$	
Spreading device	Blade	Roller	Blade	Roller	Blade	Roller
$\Pr(\lvert\zeta\rvert < 20^\circ)$	0.447	0.464	0.618	0.615	0.510	0.500
$\sigma_{\text{DEV}}(Pr)$	0.057	0.044	0.014	0.015	0.083	0.089

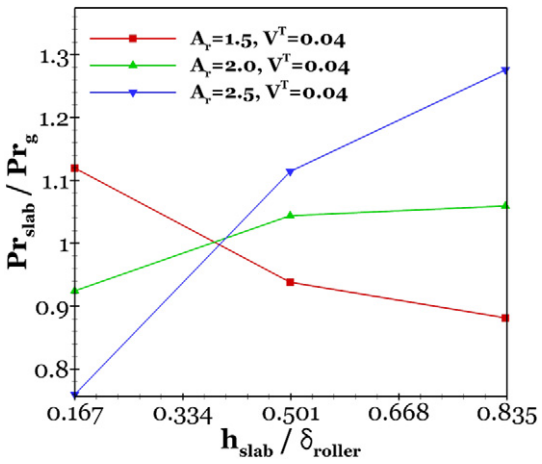

Fig. 10. Particle shape segregation after the spreading process. Only the results for $V^T_{\text{roller}} = 0.04$ are presented.

Acknowledgement

The authors gratefully acknowledge the support from the UK Engineering and Physical Sciences Research Council (EPSRC) for the present work under EP/L017318/1 and EP/L017539/1. We also acknowledge the use of the ARCHER UK National Supercomputing Service (Projects D111, E504) for conducting the simulations (http://www.archer.ac.uk). All data created during this research are openly available from the University of Strathclyde Pure/KnowledgeBase at http://doi.org/10.15129/c5993a8f-812d-46cf-bef5-92e985d12446.

References

[1] X. Yan, P. Gu, A review of rapid prototyping technologies and systems, Comput. Aided Des. 28 (1996) 307–318.
[2] I. Gibson, D.W. Rosen, B. Stucker, Additive Manufacturing Technologies, Springer. 2010.
[3] T.I. Zohdi, Additive particle deposition and selective laser processing - a computational manufacturing framework, Comput. Mech. 54 (2014) 171–191.
[4] S. Berretta, O. Ghita, K. Evans, Morphology of polymeric powders in laser sintering (LS): from polyamide to new peek powders, Eur. Polym. J. 59 (2014) 218–229.
[5] S. Ziegelmeier, P. Christou, F. Wöllecke, C. Tuck, R. Goodridge, R. Hague, E. Krampe, E. Wintermantel, An experimental study into the effects of bulk and flow behaviour of laser sintering polymer powders on resulting part properties, J. Mater. Process. Technol. 215 (2015) 239–250.
[6] J. Johanson, A rolling theory for granular solids, ASME J. Appl. Mech. 32 (1965) 842–848.
[7] R. T-Dec, A. Zavaliangos, J. Cunningham, Comparison of various modeling methods for analysis of powder compaction in roller press, Powder Technol. 130 (2003) 265–271.
[8] Y. Shanjani, E. Toyserkani, Material spreading and compaction in powder-based solid freeform fabrication methods: mathematical modeling, 19th Annual International Solid Freeform Fabrication Symposium, SFF 2008, 2008, pp. 399–410.
[9] Y. Wang, D. Rouholamin, R. Davies, O. Ghita, Powder characteristics, microstructure and properties of graphite platelet reinforced poly ether ether ketone composites in high temperature laser sintering (HT-LS), Mater. Des. 88 (2015) 1310–1320.
[10] Y. Wang, E. James, O. Ghita, Glass bead filled polyetherketone (PEK) composite by high temperature laser sintering (HT-LS), Mater. Des. 83 (2015) 545–551.
[11] E. Parteli, T. Pöschel, Particle-based simulation of powder application in additive manufacturing, Powder Technol. 288 (2016) 96–102.
[12] Z. Xiang, M. Yin, Z. Deng, X. Mei, G. Yin, Simulation of forming process of powder bed for additive manufacturing, J. Manuf. Sci. Eng. 138 (2016) 081002.
[13] M. Schmidt, D. Pohle, T. Rechtenwald, Selective laser sintering of PEEK, CIRP Ann. Manuf. Technol. 56 (2007) 205–208.
[14] M.A. Beard, O.R. Ghita, J. Bradbury, S. Flint, K.E. Evans, Material characterisation of additive manufacturing components made from a polyetherketone (PEK) high temperature thermoplastic polymer., Innovative Developments in Virtual and Physical Prototyping, 2011, pp. 329–332.
[15] O.R. Ghita, E. James, R. Trimble, K.E. Evans, Physico-chemical behaviour of poly ether ketone (PEK) in high temperature laser sintering (HT-LS), J. Mater. Process. Technol. 214 (4) (2014) 969–978.
[16] M. Vaezi, S. Yang, Extrusion-based additive manufacturing of PEEK for biomedical applications, Virtual Phys. Prototyping 10 (2015) 123–135.
[17] P. Peyre, Y. Rouchausse, D. Defauchy, G. Régnier, Experimental and numerical analysis of the selective laser sintering (SLS) of PA12 and PEKK semi-crystalline polymers, J. Mater. Process. Technol. 225 (2015) 326–336.
[18] C.A. Schneider, W.S. Rasband, K.W. Eliceiri, NIH Image to ImageJ: 25 years of image analysis, Nat. Methods 9 (2012) 671–675.
[19] S. Plimpton, Fast parallel algorithms for short-range molecular dynamics, J. Comput. Phys. 117 (1995) 1–19.
[20] A. Di Renzo, F. Di Maio, Comparison of contact-force models for the simulation of collisions in DEM-based granular flow codes, Chem. Eng. Sci. 59 (2004) 525–541.
[21] Y. Zhou, B. Wright, R. Yang, B. Xu, A. Yu, Rolling friction in the dynamic simulation of sandpile formation, Physica A 269 (1999) 536–553.
[22] J. Ai, J. Chen, J. Rotter, J. Ooi, Assessment of rolling resistance models in discrete element simulations, Powder Technol. 206 (2011) 269–282.
[23] C. Wensrich, A. Katterfeld, Rolling friction as a technique for modelling particle shape in DEM, Powder Technol. 217 (2012) 409–417.
[24] A comprehensive review of the materials properties of VICTREX® PEEK™ high performance polymer, Technical Report, VICTREX. 2016.
[25] J. Shäfer, S. Dippel, D. Wolf, Force schemes in simulations of granular materials, J. Phys. I 6 (1996) 5–20.
[26] K. Kanatani, Distribution of directional data and fabric tensors, Int. J. Eng. Sci. 22 (1984) 149–164.
[27] A. Baule, R. Mari, L. Bo, L. Portal, H.A. Makse, Mean-field theory of random close packings of axisymmetric particles, Nat. Commun. 4 (2013) 2194.
[28] W. Man, A. Donev, F.H. Stillinger, M.T. Sullivan, W.B. Russel, D. Heeger, S. Inati, S. Torquato, P.M. Chaikin, Experiments on random packings of ellipsoids, Phys. Rev. Lett. 94 (2005) 198001.
[29] Y. Guo, C. Wassgren, B. Hancock, W. Ketterhagen, J. Curtis, Granular shear flows of flat disks and elongated rods without and with friction, Phys. Fluids 06334 (2013) 1–25.
[30] Y. Guo, C. Wassgren, W. Ketterhagen, B. Hancock, B. James, J. Curtis, A numerical study of granular shear flows of rod-like particles using the discrete element method, J. Fluid Mech. 713 (2012) 1–26.